Research Square

Preprints are preliminary reports that have not undergone peer review.
They should not be considered conclusive, used to inform clinical practice,
or referenced by the media as validated information.

In-Situ Passive Infrared Thermography Application for the Assessment of Localized Mechanical Properties of TIG-Welded Inconel 625 Alloys

Nathir A Rawashdeh (narawash@mtu.edu)
Michigan Technological University https://orcid.org/0000-0002-9118-9317
Anas M Atieh
German Jordanian University
Diala Bani-Mostafa
German Jordanian University

Research Article

Keywords: Non-destructive materials characterization, thermal image, infrared thermography, TIG welding, Inconel 625

Posted Date: March 1st, 2021

DOI: https://doi.org/10.21203/rs.3.rs-235529/v1

License: This work is licensed under a Creative Commons Attribution 4.0 International License. Read Full License

Abstract

Traditional evaluation of weld joint mechanical properties by destructive testing shows the limitations of these evaluation methods, including equipment limitations, high materials/testing cost, and challenging repeatability. This work presents an experimental approach for utilizing passive infrared thermography and tensile testing to evaluate the correlation between thermal and localized TIG-welded Inconel 625 joints' mechanical properties. The results show that different areas of interest behave differently during the tensile test. The dog-bone shaped TIG-welded samples were divided into five regions of interest on both sides of the weldment, of which two are repetitive on both sides of the sample representing Inconel 625 base metal alloy, heat-affected zones, and weld beads. The temperature change rate in these three regions varied from 0.17^{o}C/min to 0.67^{o}C/min as the tensile test progresses. The fractography analysis showed that the failure occurred within the weld beads, even though the highest temperature was observed in the heat-affected zones, suggesting higher strength in the heat-affected zones. This work's suggested evaluation method provides a powerful industrial and experimental tool to predict weld failure based on temperature changes during static loading.

Introduction

Thermography is an analysis technique for materials based on capturing and analyzing thermal images using an infrared camera. It can be active or passive. For active thermography, the object under measurements is heated using an external source such as microwave, UV, and laser beam based thermal excitation [1–3]. Conversely, passive thermography does not require an external heat source. The thermal radiation originates in the object in response to thermal energy dissipation [4, 5], such is the case in this work, where tensile mechanical deformation is utilized to break the interatomic bond and resulted in materials energy dissipations.

Thermography gained increased attention in the last decade as a non-destructive tool that overcomes traditional techniques. It provides coverage for a large area of interest, spans full-field information, requires no tool for testing specimens contact, and a fast based process [6–9]. It has been used to detect small surface cracks and porosity in metal plate welds between 5–10 μm wide [10–14]. Thermography can be used for the detection of corrosion, fatigue defects and damage [15, 16]. A relation between specimen mechanical properties and thermographic images for subsurface damage propagation for mechanically quasi-static and cyclic loaded specimens of bonded repairs, temperature and phase differences and an indicator for the damage location was generated by active and passive thermographic methods [4]. In previous work, non-destructive inspection using optical cameras has been utilized for different industrial applications, including pharmaceutical and aeronautical [17, 18].

In recent work by Tuo *et al.*, thermography techniques evaluated delamination damage evolution in impacted composite laminates during compression fatigue testing [19]. Shah and Liu used thermography for real-time temperature measurements in a novel ultrasonic-assisted spot welding approach [20]. While Absi Alfaro *et al.* apply it to real-time monitoring of welding defects, i.e. humping around the arc and weld pool, the influence of the arc current and welding speed was detected for the creation of humping defects utilizing the temperature distribution generated during GTA welding, isotherm geometry and digital image processing [21]. The High-cycle fatigue life of magnesium alloy Mg-AZ31, fatigue damage, and temperature development in weld joints was predicted utilizing infrared thermography [22]. A similar methodology was utilized for monitoring the heat generation in Ti-6Al-4V alloy during linear friction stir welding [23].

Inconel 625 is a Nickel-Chromium-Molybdenum alloy that features an outstanding corrosion resistance phenomenon in a wide range of corrosive media [24]. Inconel 625 exhibits high tensile and creep strength, high corrosion fatigue strength, excellent weldability and high oxidation resistance [25–27]. It has been widely used in many engineering applications in the aerospace, nuclear and petrochemical processing industries due to chemical stability under severe chemical environment [28, 29].

Tungsten Inert Gas (TIG) welding is most commonly used with Inconel and results in joints characterized by high-strength and fabricability [30]. The presence of molybdenum and niobium within the Ni-Cr matrix affects the Inconel alloy in two ways. First, it has a wide range of service temperatures from cryogenic 982^{o}C. At room temperature for Inconel 625, the as-rolled tensile strength range from 827 to 1103 MPa, the melting temperature range from 1290 to 1350 ^{o}C, and Rockwell A hardness range from 52 to 72 HR-A. On the other hand, the tensile strength of annealed Inconel 625 may drop from 900 MPa to 100 MPa upon the increase of service temperature from 650 to 1090^{o}C [31]. Second, Inconel 625 has a strong resistivity for different corrosion types, such as chlorides-ion stress corrosion cracking, fatigue corrosion, stress cracking, oxidation, carburization and pitting corrosion cracking [32–34].

A typical welding issue of Inconel 625 is the reduction of mechanical properties and corrosion resistance in the weld beads area, which includes full penetration in the joint zone, where higher power is needed to overcome this issue [30]. Increased nugget size and less grain refinement could be observed in Inconel 625 welding, and hence an optimized process type and parameters are needed to produce a sound joint [35, 36]. This study investigates passive thermography application to detect the thermal-mechanical correlation during slow tensile loading in TIG welded Inconel 625 alloy.

Materials And Experimental Procedure

Commercially available Inconel 625 alloy was used in this study. It was obtained from (JOAMCO, Jordan) in the form of a 10 mm thick plate. The chemical composition of the Inconel 625 is shown in Table 1.

Table 1: Composition of Inconel Alloy 625 in wt.%

Element	Nickel	Chromium	Molybdenum	Iron	Tantalum	Manganese	Silicon	Cobalt	Aluminum
wt.%	Bal.	21.5	9.0	5.0	3.15	0.5	0.5	1.0	0.4

The Inconel 625 plates were halved, and edge machined to a V-shape. These edges were then manually TIG welded at a constant speed using an Inconel N82/125/10ts electrode at an approximate distance of 2 mm away from the workpiece under a shield of pure Argon (99.99%). Seven weld passes were necessary to weld the plate halves, of which five passes filled the V-shape from the upper side, and two passes completed the bead from the backside to avoid plate bending. During the upside weld passes, the current ranged from 77 to 130 Ampere. Cleaning, metal brushing and grinding were performed after each pass to remove slag and surface contaminants. The backside weld passes were performed at higher current ranges between 120 and 130 Ampere, and the surface was metallic brushed after the first pass. All the welded samples were CNC machined to create dog-bone shaped test specimens according to ASTM E8/E8M-15a standards. Tensile loading was performed at a Universal Testing Machine (Testometric FS300CT-2054, England, UK) with a 0-300 kN load cell range at a constant crosshead speed of 1.0 mm/min.

Five regions of interest were identified at the Inconel 625 welded samples, as shown in Figure 1. The regions were marked as AB, EF for base metal alloy, BC, DE for the heat-affected zones, and CD for the weld bead.

For passive thermography, we used an infrared camera (FLIR E60) with a resolution of 320 by 240 pixels and a measurement range from –10 to +120 degrees Celsius. The Thermal sensitivity is 0.05 degrees at 30 degrees Celsius, and the accuracy is ±2% of the reading. The thermal sensor is equipped with an optical 3.1 Megapixel camera of resolution 2048 by 1536 pixels and image processing software to measure object temperature profiles. The thermographic frame pictures were captured at an exposure time of 1/59 seconds and a rate of 2 frames/minute.

Figure 2 shows the complete setup for IR-Camera, Inconel 625 specimen, and UTS machine testing set up. The IR camera was positioned 1 meter away from the sample and maintained a spatial resolution of 320 by 240 pixels and a frame rate

of 2 per minute, at an integration time of 17 milliseconds. With this setup, a noise equivalent temperature difference of 50 millikelvins was maintained.

A digital watch for recording time, and a 0.8 mm gauge scaling wire to convert pixel to millimetres, were used. The spatial resolution was 0.6 mm/pixel, resulting in a scaling factor of P = 0.167 pixels/mm.

Figure 3 illustrates the methodology of this work, including data collection, analysis and interpretation. The tensile loading is performed on the Inconel 625 specimen while recording the traditional stress-strain curve using the universal testing machine force measuring load cell. In parallel, while the specimen is deforming, the in-situ thermography is recording time-stamped thermal images. After the sample failure, the tensile test concludes, and the traditional stress-strain curve is analyzed to define the mechanical behaviour, elastic and fracture limits, then the produced fractured surface is analyzed. The thermal images are also analyzed, as they show temperature time-profiles of various regions of interest for the sample under testing. This information is then correlated with the data from the stress-strain curve to gain a detailed insight into the sample's deformation in a way where local thermal signatures and mechanical properties agree.

Results And Discussion

Besides recording the sample regions' localized temperature, the thermal image helps identify the region borders because there is a thermal contrast between them. For example, to identify the weld bead region length, C & D's image coordinates must be extracted. The thermal image is viewed as a matrix of intensities corresponding to temperature, where the upper left image pixel has the row-column index zero-zero. Then the weld region's absolute total length in millimeters, for a given time t, can be calculated using the formula:

$$L_{CD}^{t} = \frac{R_D^t - R_C^t}{P} \qquad \text{..... equation (1)}$$

where R_C and R_D are the lower and upper image row indices, in pixels, of the lower and upper borders of the weld bead (CD) region, and $P = 1.67$ pixels/mm is the scaling factor of the thermal image found by measuring an object in the image such as the scale wire or the Inconel 625 sample width both in reality (in mm) and in the thermal image (in pixels):

$$P = \frac{W_{pix}}{W_{mm}} \qquad \text{..... equation (2)}$$

Equation 1 is applied in the same manner to find the elongations of all five regions AB, BC, CD, DE, and EF, for every time instance t of interest. Given the instantaneous L^t lengths of these regions, it is possible to calculate the region lengths as a percentage of the sample's overall length at a given moment. For example, the weld bead has the relative length at a given time t, of:

$$\%L_{CD}^{t} = 100 \times \frac{L_{CD}^{t}}{L_{AB}^{t} + L_{BC}^{t} + L_{CD}^{t} + L_{DE}^{t} + L_{EF}^{t}} \qquad \text{..... equation (3)}$$

The bar chart in Figure 5 illustrates the linear increase in total specimen length as the tensile test progresses, from the initial 72.3 mm to 106.4 mm when the specimen fractured. The total specimen length is composed of the localized region length, for instance, the base metal regions AB and EF, the heat-affected zone regions BC and DE, and finally, the weld bead CD. It can be observed that the value of length increase varies across the regions, which was attributed to the difference in mechanical properties and initial length.

This work also focused on the details of surface temperature evolution over the specific regions of the weld joints, heat-affected zone, and Inconel 625 base metal alloys. In other words, the question we asked: does the temperature evolution

vary across the three central regions of interest: Inconel 625 base metal alloy, heat-affected zone, and weld beads, which may show a correlation to different mechanical properties of those regions. Hence, the temperature versus time was recorded for each region as marked in the methodology in-situ during tensile loaded and then analyzed the thermographic images and its correlated time, as shown in Fig. 7. A similar approach was conducted between elongation and time. It was observed that the temperature for the heat-affected and weld beads regions (BC & CD) rises abruptly right before sample failure. This was consistent with the observation that the most deformation in these regions resulted in the highest heating rate. Simultaneously, the temperature evolution for the heat-affected and weld bead zones was higher than the Inconel 625 base metal alloy, which was also consistent with the deformation profile. It was speculated that the difference in temperature development was due to the difference in mechanical behaviour where the weld beads and heat-affected zone show more ductile behaviour compared to a more brittle and rigid (plastic) behaviour in the base metal alloy. With this, it was concluded that the Inconel 625 TIG-welded specimens exhibit two behaviours of elastic and plastic acting parallel on the net specimen deformation.

As seen in the figure, the heat-affected zone (BC) is always slightly warmer than the weld bead (CD) as the tensile test progresses, indicating it is more plastic than the weld bead. The weld bead's temporal temperature profiles (CD) and heat-affected zone (BC) exhibit a similar trend as the tensile test progresses. There are four distinct regions of the temperature change rate. Namely: 0 to 4.5 min, 4.5 to 14 min, 14 to 32 min, and 32 to 34 min. The slopes of these four regions, m_1 = 0.17°C/min, m_2 = 0.39°C/min, m_3 = 0.19°C/min, and m_4 = 0.67°C/min, correspond to the weld bead’s (region CD) rate of temperature change, and plastic deformation throughout the tensile test. With this understanding, it becomes possible to predict the specimen's fracture time. In the case under study, the fracture occurred about 2.5 minutes after the weld bead heating rate rose to the level of m_4. The same discussion applies to the heat-affected zone (BC region). The base metal (AB region) temperature rates of change, on the other hand, are distinguishable for the other two zones after the second inflection point at 14 minutes.

This indicates three inflection times at T_1 = 4.6, T_2 = 14, and T_3 = 32 minutes, corresponding to the entire sample's mechanical behaviour shown in Fig. 8. The maximum temperature profile shown corresponds to the heat-affected zones (BC & EF) and the weld bead (CD). There is a clear indication that the three inflection times, which were deduced from the thermal data, correlate to the mechanical stress curve's inflection points. In the last inflection point T_3, the weld bead hardens, and shortly after that, at minute 34, the fracture occurs.

After the fracture, specimen images were directly captured using a light optical microscope to show the fracture profile, the type of fracture, either ductile or brittle and to see where the fracture took place. It is well established in the research literature that a fracture with extensive plastic deformation and energy absorption before the failure is ductile. Hence, a ductile fracture surface usually has coarser precipitates mixed with flat groves and subtle dimples. Therefore, the coarse slip bands are then formed over the crack path. On the other hand, a brittle fracture shows little plastic deformation and low energy absorption before it occurs. When the material has high strengths, the fracture and cracks paths occur intergranularly, a flatter surface is observed. Figure 9 shows the thermal and optical images of the Inconel 625 after fracturing, and it can be concluded that fracture occurred precisely in the middle third of the weld bead. It is speculated that the fracture path and surface profile correspond to a ductile fracture path, where plastic deformation occurred with coarse surface profile mixed with subtle dimples. This agrees with the observation seen in the previous discussion that weld beads are the region where most deformation occurs. It can be observed from Fig. 9 (a) that the weld bead is where the fractured progress even though the temperature was maximum at the heat-affected zones, which may mean that they are still deforming and have more rigid mechanical properties. Conversely, the Inconel 625 base metal alloy shows the lowest temperature indicating it is not deforming and can still sustain higher stress than the weld beads.

Conclusions

In situ evaluation of tensile loading and thermography was carried out for the TIG-welded Inconel 625 specimen. Thermal-mechanical correlation showed that elongation of the specimens includes both elastic and plastic deformation of different regions of interest. The temperature increase during the tensile loading was attributed to the samples' plastic deformation; however, it was observed that mechanical behaviour and temperature increase for the there regions of interest; Inconel 625 base metal alloy heat-affected zones, and weld bead vary during loading at the same time. The specimen and its different regions can be viewed as a series of springs, where elasticity is lost gradually, and the regions lose the elasticity at different rates one after the other. A significant difference in heating rate was observed, which varied from 0.17^{o}C/min to 0.67^{o}C/min as the tensile test progress. The higher rate of 0. 67^{o}C/min was observed a few minutes before failure in the heat-affected zone, which may help predict the failure early. The specimen fracture occurred precisely in the middle third of the weld beads. It is speculated that the fracture surface is a ductile fracture such that plastic deformation occurred with a coarse surface profile mixed with subtle dimples; this was in agreement with the observation that the weld beads showed the highest rate of local elongation percentage of 30% compared to other regions of interest.

Declarations

Declaration of competing interest

The authors declare that they have no known competing financial interests or personal relationships that could have influenced the work reported in this paper.

Credit author statement

Conceptualization: N.A.R & A.M.A, Thermography setup: N.A.R., D.B., Experimental Design and tensile testing: N.A.R., A.M.A, and D.B. Formal analysis: N.A.R & A.M.A, This article was written and reviewed by N.A.R & A.M.A.

References

1. Rippa M, Ambrosone A, Leone A, Mormile P. Active thermography for real time monitoring of UV-B plant interactions. J Photochem Photobiol B Biol 2020;208. https://doi.org/10.1016/j.jphotobiol.2020.111900
2. Xu Y, Hwang S, Wang Q, Kim D, Luo C, Yang J et al. Laser active thermography for debonding detection in FRP retrofitted concrete structures. NDT E Int 2020;114. https://doi.org/10.1016/j.ndteint.2020.102285
3. Zou X, Mirala A, Sneed LH, Al Qaseer MT, Donnell K (2020) Detection of CFRP-concrete interfacial debonding using active microwave thermography. Compos Struct. https://doi.org/10.1016/j.compstruct.2020.113261
4. Martens U, Schröder KU (2020) Evaluation of infrared thermography methods for analysing the damage behaviour of adhesively bonded repair solutions. Compos Struct 240:111991. https://doi.org/10.1016/j.compstruct.2020.111991
5. Harizi W, Chaki S, Bourse G, Ourak M (2014) Mechanical damage assessment of Glass Fiber-Reinforced Polymer composites using passive infrared thermography. Compos Part B Eng 59:74–79. https://doi.org/10.1016/j.compositesb.2013.11.021
6. Matteï S, Grevey D, Mathieu A, Kirchner L (2009) Using infrared thermography in order to compare laser and hybrid (laser + MIG) welding processes. Opt Laser Technol 41:665–670. https://doi.org/10.1016/j.optlastec.2009.02.005
7. Hung YY, Chen YS, Ng SP, Liu L, Huang YH, Luk BL et al (2009) Review and comparison of shearography and active thermography for non-destructive evaluation. Mater Sci Eng R Reports 64:73–112. https://doi.org/10.1016/j.mser.2008.11.001
8. Zhang HX, Wu GH, Yan ZF, Guo SF, Chen PD, Wang WX (2014) An experimental analysis of fatigue behavior of AZ31B magnesium alloy welded joint based on infrared thermography. Mater Des 55:785–791. https://doi.org/10.1016/j.matdes.2013.10.036

9. Villar M, Garnier C, Chabert F, Nassiet V, Samélor D, Diez JC et al (2018) In-situ infrared thermography measurements to master transmission laser welding process parameters of PEKK. Opt Lasers Eng 106:94–104. https://doi.org/10.1016/j.optlaseng.2018.02.016
10. Broberg P (2013) Surface crack detection in welds using thermography. NDT E Int 57:69–73. https://doi.org/10.1016/j.ndteint.2013.03.008
11. Światczak T, Tomczyk M, Wiecek B, Pawlak R, Olbrycht R (2012) Defect detection in wire welded joints using thermography investigations. Mater Sci Eng B Solid-State Mater Adv Technol 177:1239–1242. https://doi.org/10.1016/j.mseb.2012.03.009
12. Javadi Y, Mohseni E, MacLeod CN, Lines D, Vasilev M, Mineo C et al (2020) Continuous monitoring of an intentionally-manufactured crack using an automated welding and in-process inspection system. Mater Des 191:108655. https://doi.org/10.1016/j.matdes.2020.108655
13. Rodríguez-Martin M, Lagüela S, González-Aguilera D, Arias P (2014) Cooling analysis of welded materials for crack detection using infrared thermography. Infrared Phys Technol 67:547–554. https://doi.org/10.1016/j.infrared.2014.09.025
14. Rodríguez-Martín M, Lagüela S, González-Aguilera D, Martinez J (2015) Prediction of depth model for cracks in steel using infrared thermography. Infrared Phys Technol 71:492–500. https://doi.org/10.1016/j.infrared.2015.06.013
15. Doshvarpassand S, Wu C, Wang X (2019) An overview of corrosion defect characterization using active infrared thermography. Infrared Phys Technol 96:366–389. https://doi.org/10.1016/j.infrared.2018.12.006
16. Ummenhofer T, Medgenberg J (2009) On the use of infrared thermography for the analysis of fatigue damage processes in welded joints. Int J Fatigue 31:130–137. https://doi.org/10.1016/j.ijfatigue.2008.04.005
17. Atieh A, Rawashdeh N, AlHazaa A (2018) Evaluation of Surface Roughness by Image Processing of a Shot-Peened, TIG-Welded Aluminum 6061-T6 Alloy: An Experimental Case Study. Materials (Basel) 11:771. https://doi.org/10.3390/ma11050771
18. Rawashdeh NA, Abu-Khalaf JM, Khraisat W, Al-Hourani SS (2018) A visual inspection system of glass ampoule packaging defects: effect of lighting configurations. Int J Comput Integr Manuf 31:848–856. https://doi.org/10.1080/0951192X.2018.1447145
19. Tuo H, Wu T, Lu Z, Ma X (2021) Evaluation of damage evolution of impacted composite laminates under fatigue loadings by infrared thermography and ultrasonic methods. Polym Test 93:106869. https://doi.org/10.1016/j.polymertesting.2020.106869
20. Shah U, Liu X (2020) Effect of ultrasonic energy on the spot weldability of aluminum alloy AA6061. Mater Des 192:108690. https://doi.org/10.1016/j.matdes.2020.108690
21. Alfaro SCA, Vargas JAR, De Carvalho GC, De Souza GG (2015) Characterization of "humping" in the GTA welding process using infrared images. J Mater Process Technol 223:216–224. https://doi.org/10.1016/j.jmatprotec.2015.03.052
22. Xiao-qing L, Hong-xia Z, Zhi-feng Y, Wen-xian W, Ya-guo Z, Qian-ming Z (2013) Fatigue life prediction of AZ31B magnesium alloy and its welding joint through infrared thermography. Theor Appl Fract Mech 66–67:46–52. https://doi.org/10.1016/j.tafmec.2013.10.001
23. Maio L, Liberini M, Campanella D, Astarita A, Esposito S, Boccardi S et al (2017) Infrared thermography for monitoring heat generation in a linear friction welding process of Ti6Al4V alloy. Infrared Phys Technol 81:325–338. https://doi.org/10.1016/j.infrared.2017.01.023
24. Chen TC, Chou CC, Yung TY, Cai RF, Huang JY, Yang YC (2020) A comparative study on the tribological behavior of various thermally sprayed Inconel 625 coatings in a saline solution and deionized water. Surf Coatings Technol 385:125442. https://doi.org/10.1016/j.surfcoat.2020.125442

25. Sun Y, Chen L, Li L, Ren X (2020) High-temperature oxidation behavior and mechanism of Inconel 625 super-alloy fabricated by selective laser melting. Opt Laser Technol 132:106509. https://doi.org/10.1016/j.optlastec.2020.106509
26. Sun R, Shi Y, Yang Y, Wang X, Zhou X (2021) Microstructure, element segregation and performance of Inconel 625 metal layer deposited by laser assisted ultra-high frequency induction deposition. Surf Coatings Technol 405:126715. https://doi.org/10.1016/j.surfcoat.2020.126715
27. Alvarães CP, Jorge JCF, de Souza LFG, Araújo LS, Mendes MC, Farneze HN. Microstructure and corrosion properties of Single Layer Inconel 625 Weld Cladding Obtained by the Electroslag Welding Process. J Mater Res Technol 2020;9. https://doi.org/10.1016/j.jmrt.2020.11.048
28. Tripathy M, Munther M, Davami K, Beheshti A (2020) Surface property study of additively manufactured Inconel 625 at room temperature and 510°C. Manuf Lett 26:69–73. https://doi.org/10.1016/j.mfglet.2020.10.001
29. Yenusah CO, Ji Y, Liu Y, Stone TW, Horstemeyer MF, Chen LQ et al (2021) Three-dimensional Phase-field simulation of γ" precipitation kinetics in Inconel 625 during heat treatment. Comput Mater Sci 187:110123. https://doi.org/10.1016/j.commatsci.2020.110123
30. Sampath Kumar S, Maheswaran CB, Bharathi Kannan TD. Experimental investigation on a pulsed TIG welding of Inconel 625. Mater Today Proc 2020. https://doi.org/10.1016/j.matpr.2020.09.724
31. Corporation SM. Inconel Alloy 625. WwwSpecialmetalsCom 2013:1–28. https://doi.org/SMC-066
32. Kumar Krovvidi SCSP, Goyal S, Bhaduri AK (2020) Design, analysis and experimental validation of Inconel-625 bellows for critical applications. Mater Today Proc. https://doi.org/10.1016/j.matpr.2020.06.303
33. Thejasree P, Manikandan N, Binoj JS, .Varaprasad KC, Palanisamy D, Raju R. Numerical simulation and experimental investigation on laser beam welding of Inconel 625. Mater Today Proc 2020:0–5. https://doi.org/10.1016/j.matpr.2020.07.042
34. Ren D, Xue Z, Jiang Y, Hu X, Zhang Y (2020) Influence of single tensile overload on fatigue crack propagation behavior of the selective laser melting inconel 625 superalloy. Eng Fract Mech 239:107305. https://doi.org/10.1016/j.engfracmech.2020.107305
35. Rezaei Ashtiani HR, Zarandooz R (2015) The Influence of Welding Parameters on the Nugget Formation of Resistance Spot Welding of Inconel 625 Sheets. Metall Mater Trans A 46:4095–4105. https://doi.org/10.1007/s11661-015-3030-1
36. Song KH, Nakata K (2010) Effect of precipitation on post-heat-treated Inconel 625 alloy after friction stir welding. Mater Des 31:2942–2947. https://doi.org/10.1016/j.matdes.2009.12.020

Figures

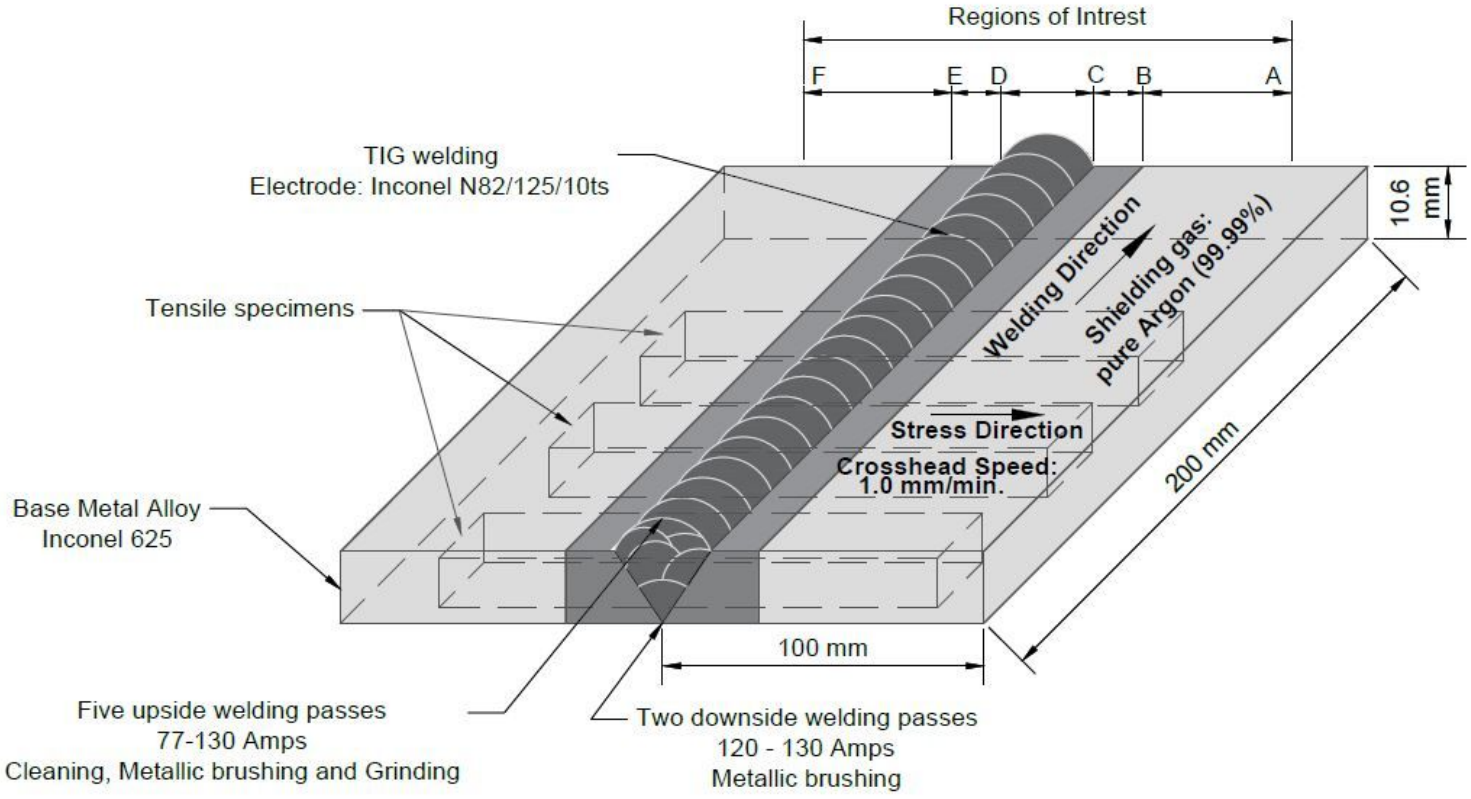


Figure 1

Welded Inconel 625 specimen showing tensile specimens and their regions of interest

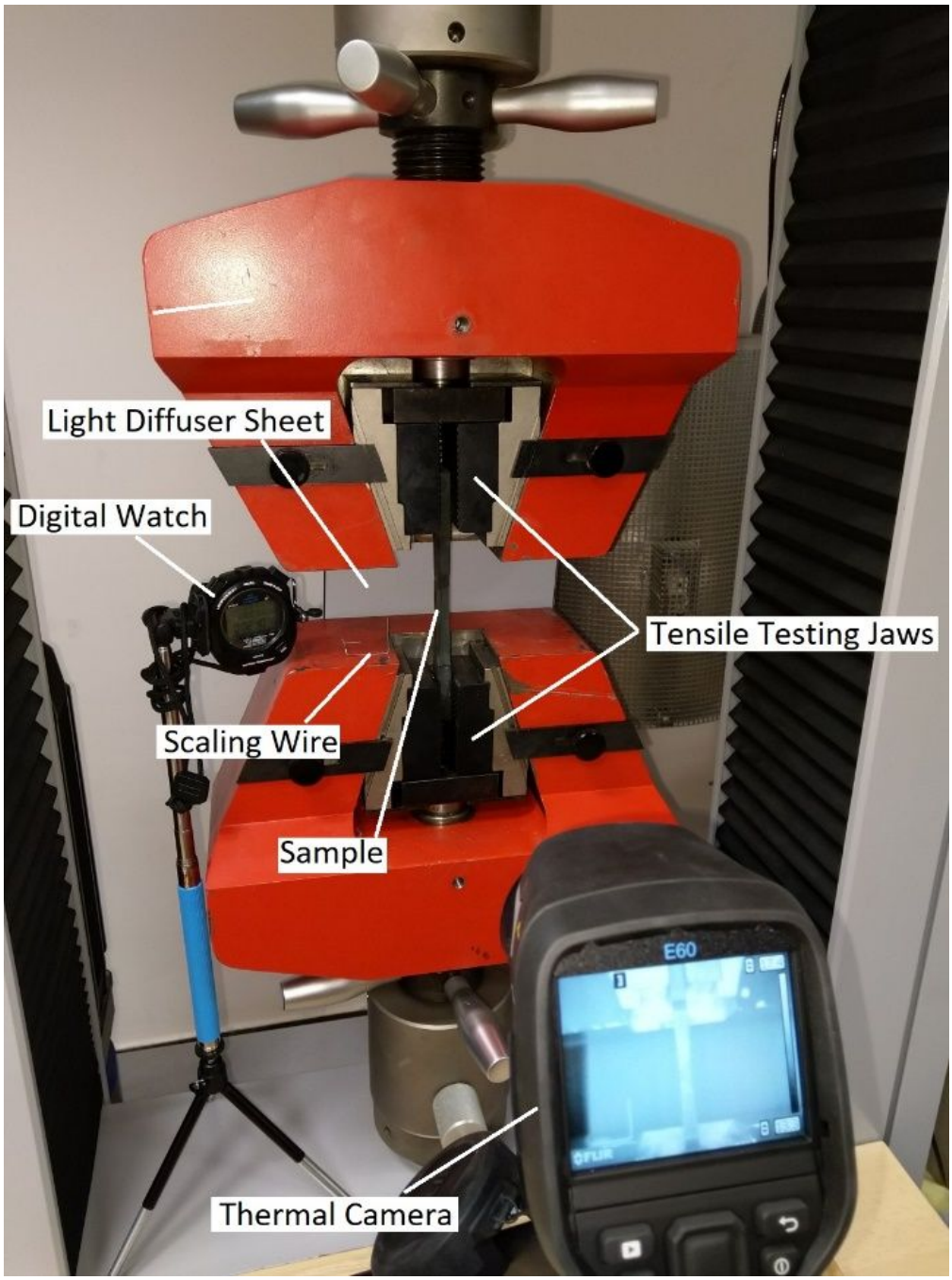


Figure 2

Complete experimental setup for tensile testing and passive thermography

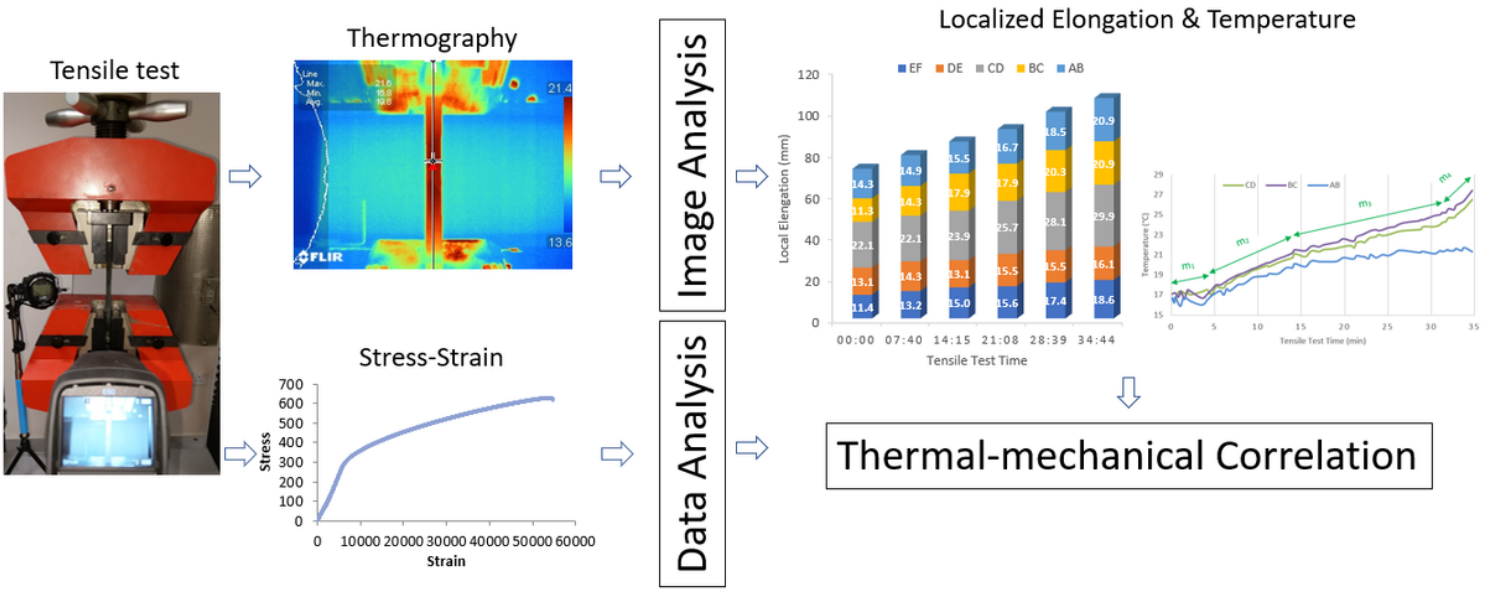


Figure 3

Schematic representation of the data collection and processing procedure followed in this research work

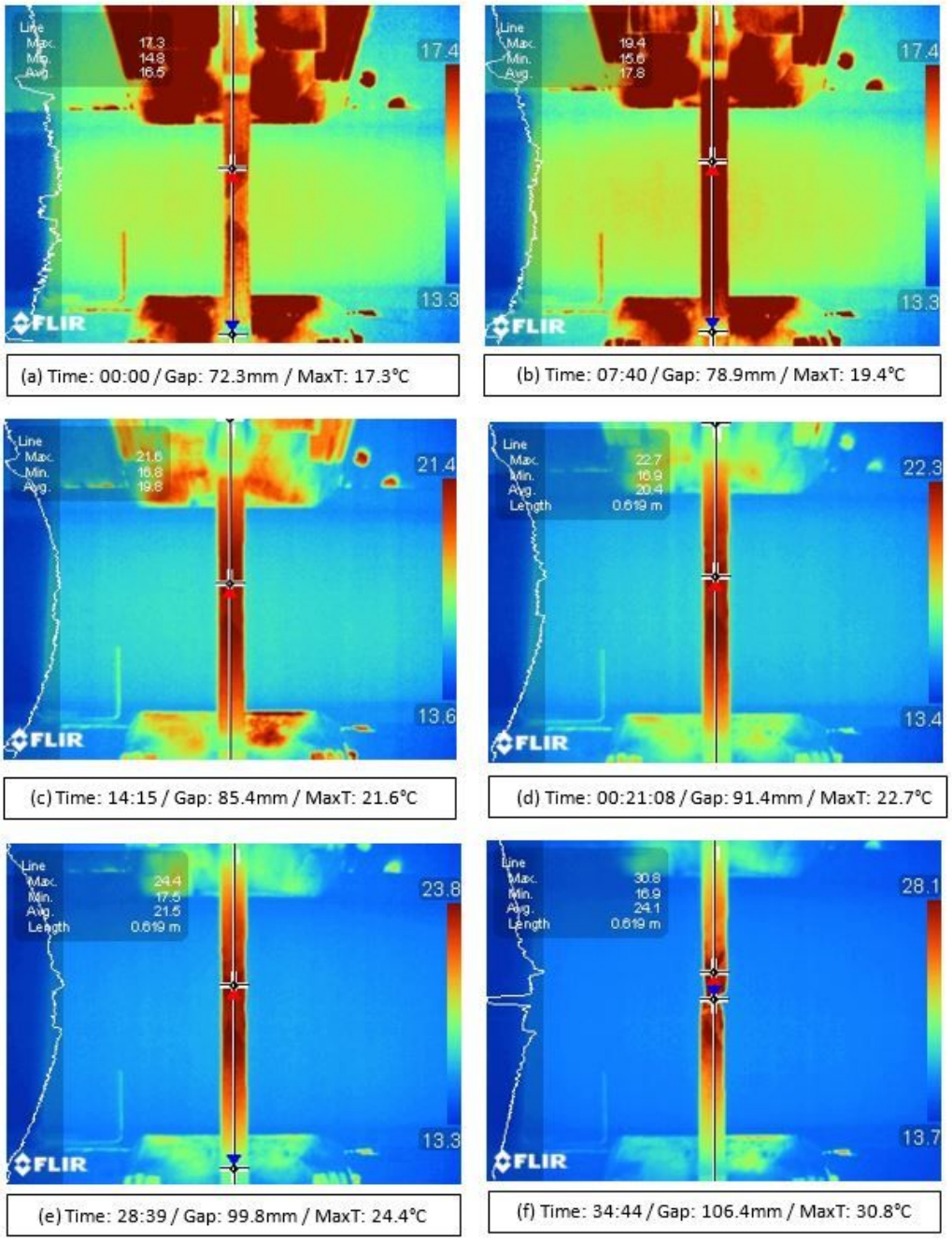


Figure 4

Thermal images selected at 7 miniute intervals for the tensile loading specimens showing the temperature profile of a vertical line over the sample length

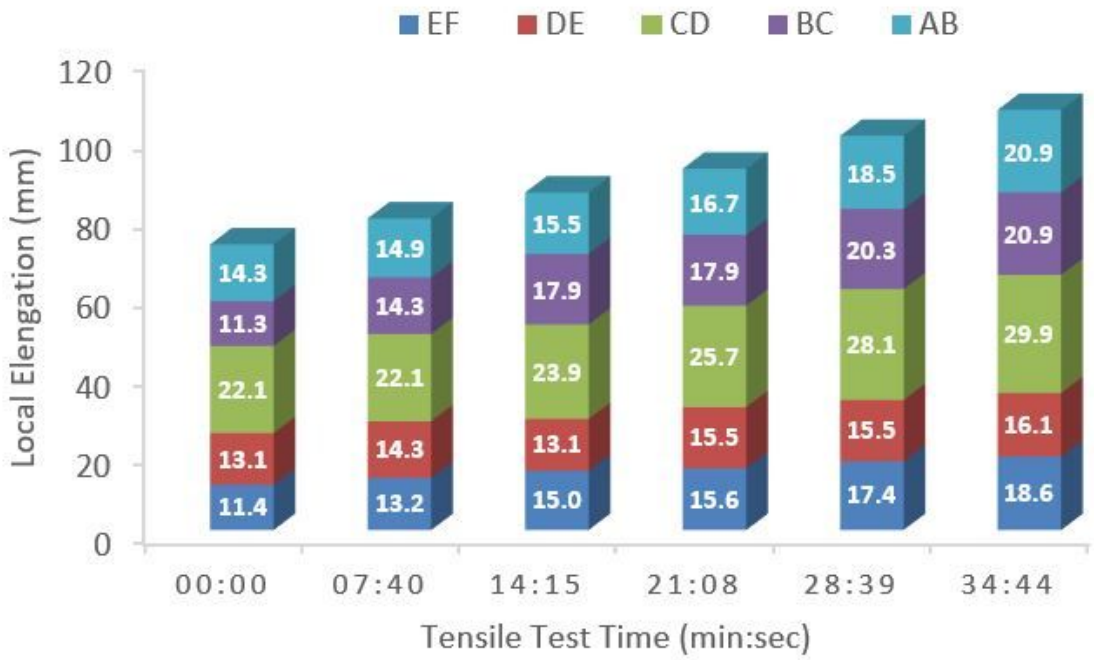


Figure 5

Total specimen and localized region elongations throughout a tensile test

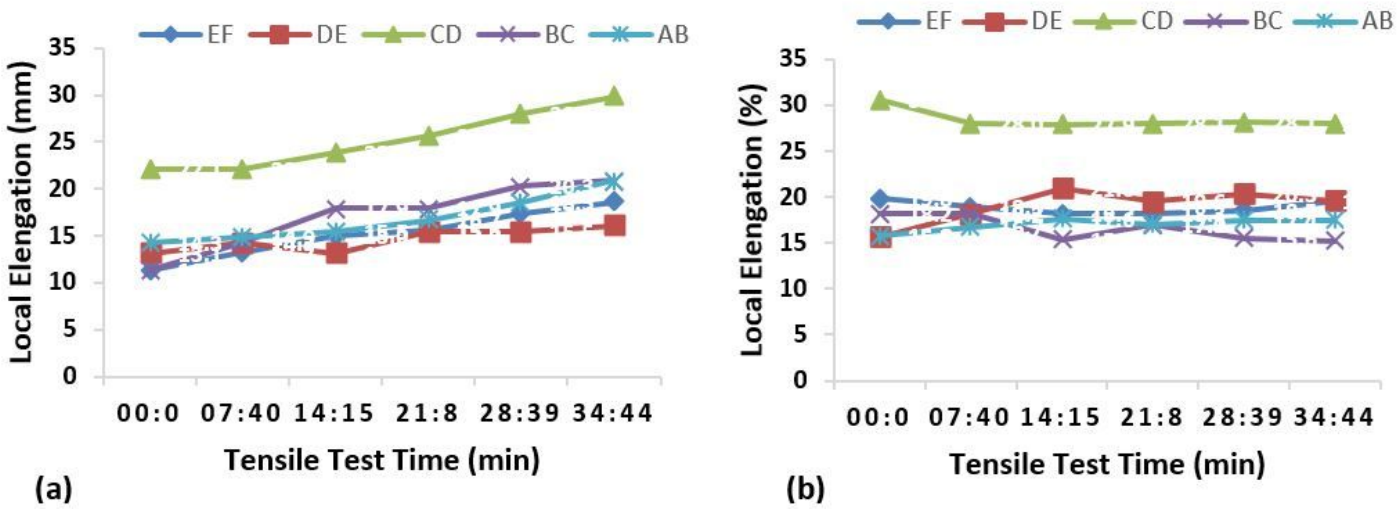


Figure 6

(a) Local elongation length in (mm) (b) Local elongation percentage (%) versus tensile loading time

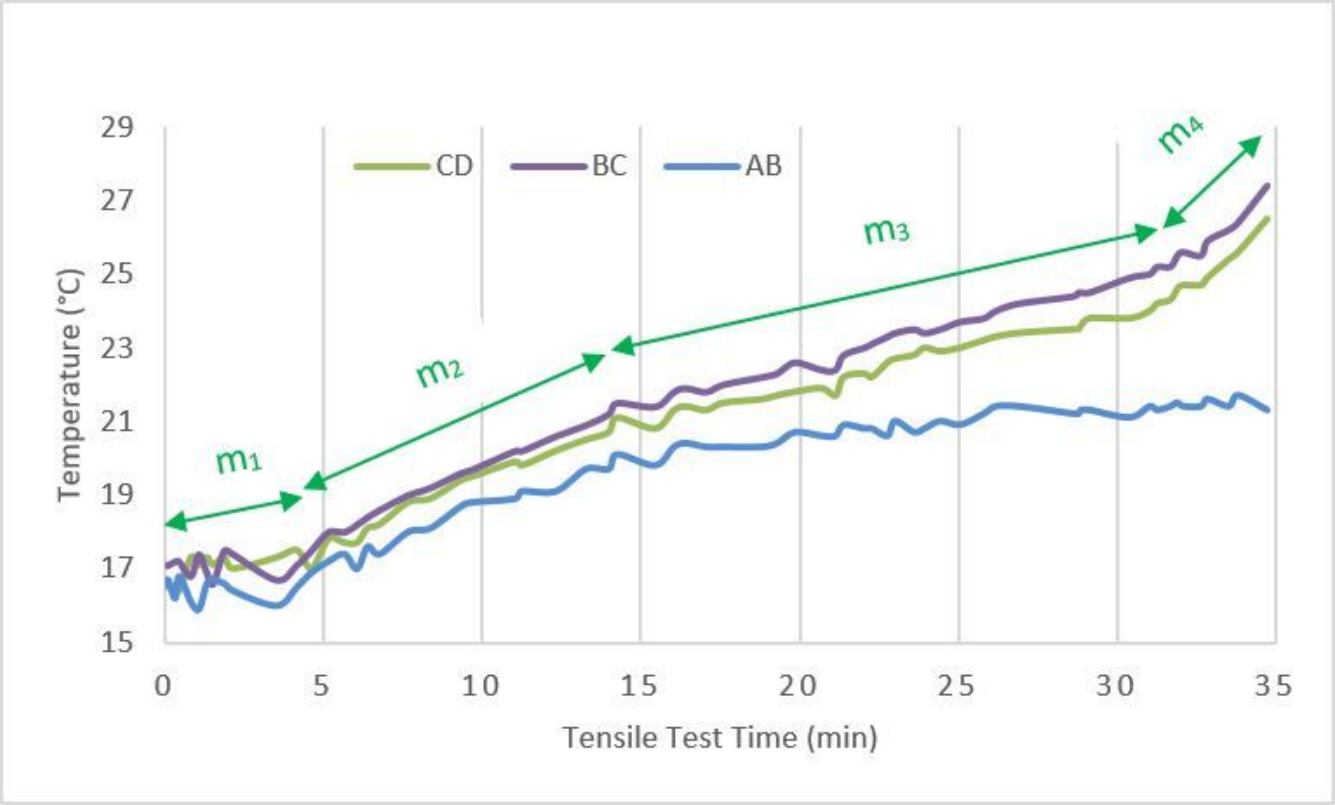


Figure 7

Localized specimen region temperatures throughout the tensile test

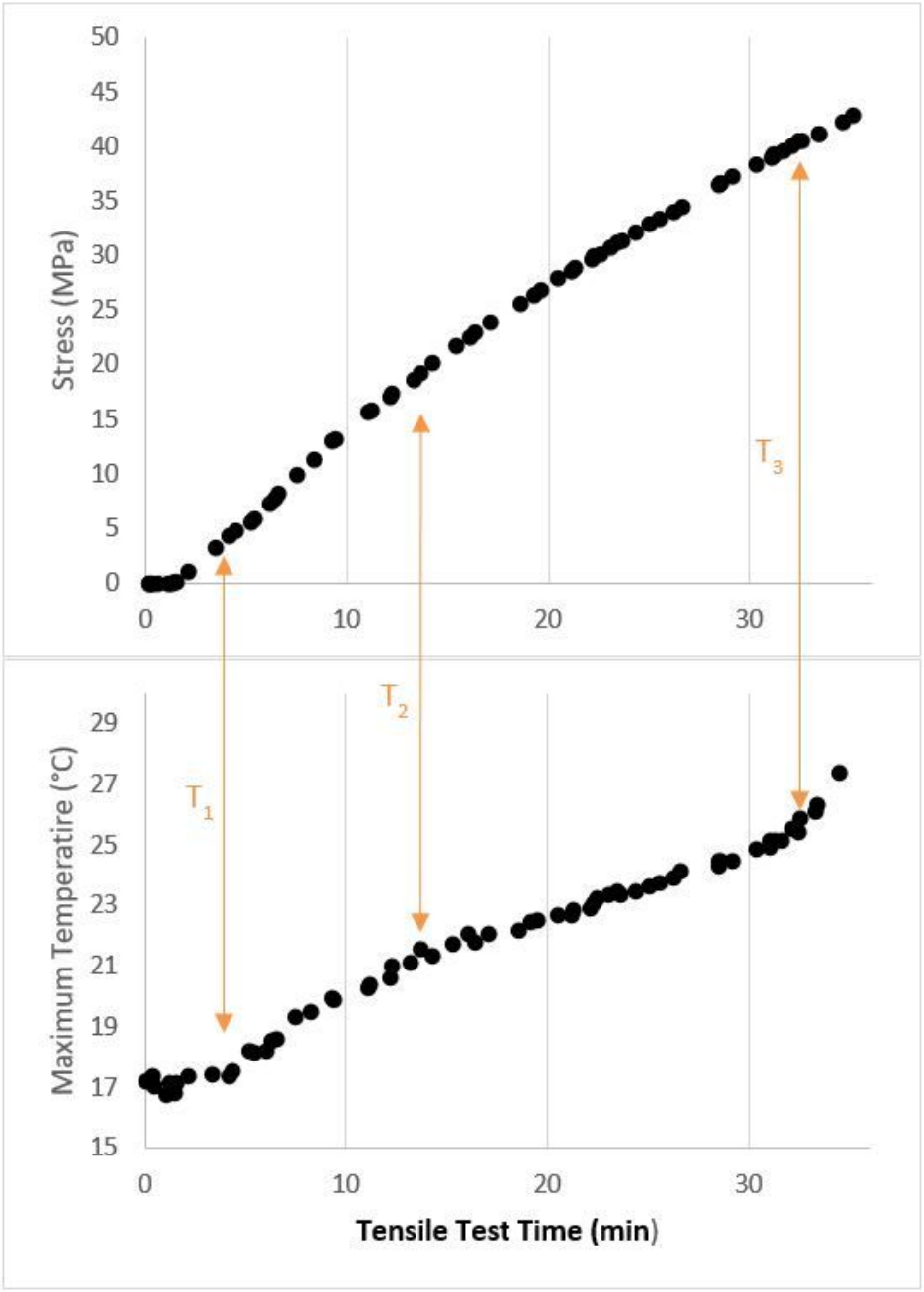


Figure 8

Tensile stress and localized temperature correlation

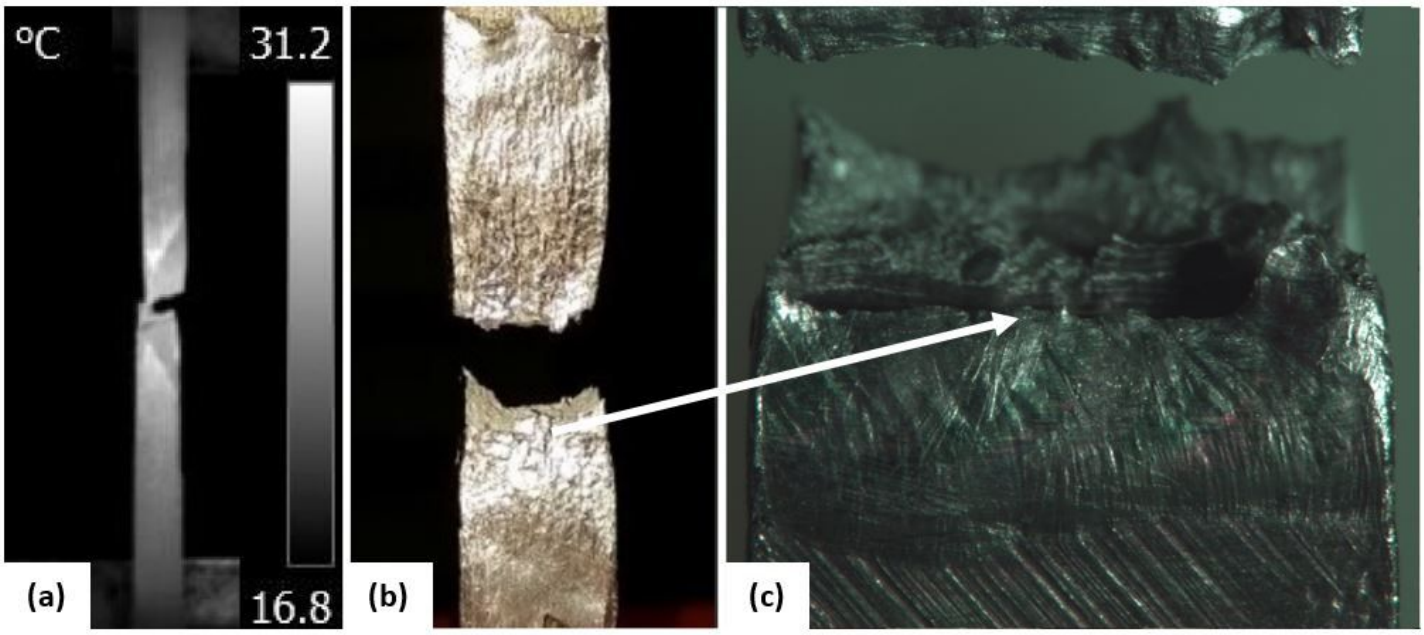


Figure 9

(a) Thermal (b) and (c) optical magnified fracture surface images